3D plane-wave migration in tilted coordinates

Guojian Shan, Robert Clapp, and Biondo Biondi

ABSTRACT

We develop 3D plane-wave migration in tilted coordinates for anisotropic media. We transform the recorded surface data to plane-wave data by slant-stack processing. Both the source plane-wave and its corresponding slant-stacked data are extrapolated into the subsurface within a tilted coordinates system whose direction depends on the propagation direction of the plane-wave. Images are generated by cross-correlating these two wavefields. A real dataset from Gulf of Mexico shows that this technique can image steeply dipping salt flanks and faults, even though the one-way wave equation operator is used for the wavefield extrapolation.

INTRODUCTION

Kirchoff migration has been widely applied in seismic processing due to its relative cheap cost and flexibility. However, it can not provide reliable images where there is strongly lateral velocity variation because of its high-frequency assumption. Wave-equation migration, which is performed by recursive wavefield extrapolation, has been demonstrated to overcome these limitations and produce better images in areas of complex geology.

It is well known that waves propagate upward and downward simultaneously. Reverse-time migration (Whitmore, 1983; Baysal et al., 1983; Biondi and Shan, 2002), which solves the full wave equation directly and mimics wave propagation naturally, is still too expensive for today's computing facilities. As a result, downward continuation methods (Claerbout, 1985), which are based on one-way wave equation wavefield extrapolation and much cheaper than reverse-time migration, are widely used in the industry.

Conventional downward continuation method extrapolates wavefields using the one-way wave equation in Cartesian coordinates. For a medium without lateral variation, the phase-shift method (Gazdag, 1978) can be applied, and one-way wave equation can model waves propagating in a direction up to $90°$ away from the extrapolation direction. But in a laterally varying medium, it is very difficult to model waves propagating in a direction far from the extrapolation direction using the one-way wave equation. A lot of effort has been made to improve the accuracy of the wavefield-extrapolation operator in laterally varying media, including Fourier finite-difference (Ristow and Ruhl, 1994; Biondi, 2002), general screen propagator (de Hoop, 1996; Huang and Wu, 1996), and optimized finite difference (Lee and Suh, 1985) with phase correction (Li, 1991). Even if we could model waves accurately up to 90 degree using the one-way wave equation in laterally varying media, overturned waves, which travel downward

first and then curve upward, are filtered away during the extrapolation. This is because only down-going waves are allowed in the source wavefield and only up-going waves are allowed in the receiver wavefield in downward continuation. But overturned waves and waves propagating in a high angle direction play a key role in imaging the steeply dipping reflectors. As a consequence, imaging steeply dipping reflectors, such as salt flank and faults, remain a major problem in downward continuation.

Some work has been done to image the steeply dipping reflectors with one-way wave equation by coordinate transformation. This includes tilted coordinates (Higginbotham et al., 1985; Etgen, 2002), the combination of downward continuation and horizontal continuation (Zhang and McMechan, 1997), or wavefield extrapolation in general coordinates such as ray coordinates (Nichols, 1994) and Riemannian coordinates (Sava and Fomel, 2005; Shragge, 2006).

Plane-wave source migration (Whitmore, 1995; Rietveld, 1995; Duquet et al., 2001; Liu et al., 2002; Zhang et al., 2005) has been demonstrated as a useful tool in seismic imaging. Shan and Biondi (2004) perform 2D plane-wave migration in tilted coordinates to image steeply dipping reflectors and overturned waves using one-way wave equation. In this paper, we develop 3D full plane-wave migration in tilted coordinates.

This paper is organized as follows: we begin with a brief review of plane-wave migration, then describe the theory of plane-wave migration in tilted coordinates, and finally demonstrate our technique with a real dataset example.

3D PLANE-WAVE MIGRATION

The original surface seismic data are usually shot gathers. A typical seismic shot gather (the receiver wavefield of a shot at the surface) is a five dimensional object: $R(s_y, s_x, r_y, r_x, z = 0, t)$, where (s_y, s_x) is the source location, (r_x, r_y) is the receiver location and t is the travel time. After a Fourier transformation in t, we have the receiver wavefield in the frequency domain $R(s_y, s_x, r_y, r_x, z = 0, \omega)$, where ω is the angular frequency.

Each shot represents a real physical experiment. The most straight forward way to obtain the image of the subsurface is shot-profile migration, in which we obtain the local image of each experiment independently and form the final image of the subsurface by stacking all the local images. A typical shot-profile migration algorithm includes two steps. First, source and receiver wavefields are extrapolated into the subsurface using one-way wave equations. In isotropic media they are defined as follows:

$$\frac{\partial S}{\partial z} = -\frac{i\omega}{v}\sqrt{1 + \frac{v^2}{\omega^2}\left(\frac{\partial^2}{\partial x^2} + \frac{\partial^2}{\partial y^2}\right)}S, \tag{1}$$

$$\frac{\partial R}{\partial z} = +\frac{i\omega}{v}\sqrt{1 + \frac{v^2}{\omega^2}\left(\frac{\partial^2}{\partial x^2} + \frac{\partial^2}{\partial y^2}\right)}R, \tag{2}$$

where $v = v(x, y, z)$ is the velocity of the media, $S = S(s_y, s_x; x, y, z, \omega)$ is the source wavefield, which is an impulse at the surface and $R = R(s_y, s_x; r_y, r_x, z, \omega)$ is the receiver wavefield.

Second, the image is formed by cross-correlating the source and receiver wavefields:

$$I(x,y,z) = \int \int \int \bar{S}(s_x,s_y;x,y,z,\omega)R(s_x,s_y;x,y,z,\omega)d\omega ds_x ds_y. \tag{3}$$

Plane-wave source migration

Shot gathers can also be synthesized to a new dataset to represent a physical experiment that does not occur in reality. One of the most important examples is to synthesize shot gathers to plane-wave source gathers. The plane-wave source gathers represent experiments that planar sources originate from all angles at the surface. They can also be regarded as the accurate phase-encoding of the shot gathers (Liu et al., 2006). The plane-wave source dataset can be generated by delaying the shot in shot gathers or slant-stacking in receiver gathers as follows:

$$R_p(p_x,p_y;r_x,r_y,z=0,\omega) = \int \int R(s_x,s_y;r_x,r_y,z=0,\omega)e^{i\omega(s_x p_x + s_y p_y)}ds_x ds_y, \tag{4}$$

where p_x and p_y are ray parameters in the in-line and cross-line directions respectively. Its corresponding plane-wave source wavefield at the surface is

$$S_p(p_x,p_y;r_x,r_y,z=0,\omega) = \int \int e^{i\omega(s_x p_x + s_y p_y)}ds_x ds_y. \tag{5}$$

Similar to the Fourier transformation, we can transform the plane-wave source data back to shot gathers by the inverse slant-stacking (Claerbout, 1985) as follows

$$R(s_x,s_y;r_x,r_y,z=0,\omega) = \int \int \omega^2 R_p(p_x,p_y;r_x,r_y,z=0,\omega)e^{-i\omega(s_x p_x + s_y p_y)}dp_x dp_y \tag{6}$$

In contrast to the inverse Fourier transformation, the kernel of the integral is weighted by the square of the frequency ω.

The source wavefield S_p and receiver wavefield R_p are extrapolated into the subsurface independently using the one-way wave equations 1 and 2. The image of a plane-wave source with a ray parameter pair (p_x, p_y) is formed by cross-correlating the source and receiver wavefields weighted with the square of the frequency ω:

$$I_{p_x,p_y}(x,y,z) = \int \omega^2 \bar{S}_p(p_x,p_y;x,y,z,\omega)R_p(p_x,p_y;x,y,z,\omega)d\omega. \tag{7}$$

The final image is generated by stacking the images of all possible plane-wave sources:

$$I_p = \int \int I_{p_x,p_y}(x,y,z)dp_x dp_y. \tag{8}$$

Because both slant-stacking and migration are linear operators, the image of the plane-wave migration I_p is equivalent to the image obtained by shot-profile migration (Liu et al., 2002; Zhang et al., 2005).

Conical-wave source migration

For narrow azimuth data, conical-wave source migration has been demonstrated as an efficient way to image the subsurface (Whitmore, 1995; Duquet et al., 2001; Zhang et al., 2005). The conical-wave source data are generated as follows

$$R_c(p_x, s_y; r_x, r_y, z = 0, \omega) = \int R(s_x, s_y; r_x, r_y, z = 0, \omega) e^{i\omega(s_x p_x)} ds_x. \tag{9}$$

And the corresponding conical source at the surface is

$$S_c(p_x, s_y; r_x, r_y, z = 0, \omega) = \int e^{i\omega(s_x p_x)} ds_x. \tag{10}$$

Similar to the plane-wave source migration, the image of a conical-wave source can be obtained by cross-correlating the source and receiver wavefields weighted with the frequency ω:

$$I_{p_x, s_y}(x, y, z) = \int \omega \bar{S}_c(p_x, s_y; x, y, z, \omega) R_c(p_x, s_y; x, y, z, \omega) d\omega, \tag{11}$$

where $S_c(p_x, s_y; x, y, z, \omega)$ and $R_c(p_x, s_y; x, y, z, \omega)$ are the conical-wave source and receiver wavefields extrapolated from the surface using equation 1 and 2. The final image is generated by stacking images of all possible conical-wave sources of all sail lines:

$$I_c = \int \int I_{p_x, s_y}(x, y, z) dp_x ds_y. \tag{12}$$

Similar to the 3D plane-wave migration, the image of conical-wave migration is equivalent to the shot-profile migration.

3D PLANE-WAVE MIGRATION IN TILTED COORDINATES

A 3D plane-wave source is specified by two ray-parameters, p_x and p_y. Given the velocity at the surface v_{z_0}, we can calculate the propagation direction of the plane-wave source at the surface from the two ray-parameters. For each plane-wave source, we rotate the Cartesian coordinates, so that the extrapolation direction of the new coordinates is close to the propagation direction of the plane-wave. In 3D, the propagation direction of a plane-wave source is defined by two angles: the azimuth angle α and the take-off angle θ. Given the velocity at the surface v_{z_0} and a plane-wave source with a ray parameter pair $(p_x\ p_y)$, its propagation direction at the surface is defined by the vector (q_x, q_y, q_z), where

$$
\begin{aligned}
q_x &= p_x v_{z_0}, & (13) \\
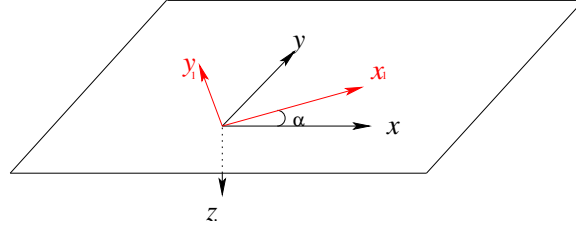q_y &= p_y v_{z_0}, & (14) \\
q_z &= \sqrt{1 - (q_x^2 + q_y^2)}. & (15)
\end{aligned}
$$

The azimuth angle and take-off angle of the plane-wave source are calculated from the vector (q_x, q_y, q_z) as follows:

$$\alpha = \arcsin(q_y/q_x), \tag{16}$$

$$\theta = \arccos(q_z). \tag{17}$$

Figure 1: Rotation about the axis z by α guojian1-rotazimuth [NR]

Rotations in 3D are specified by the axis of rotation and rotation angle. They can be described by a rotation matrix. For example, a rotation about the z-axis by an angle α (Figure 1) is

$$\begin{pmatrix} x_1 \\ y_1 \\ z_1 \end{pmatrix} = R_z(\alpha) \begin{pmatrix} x \\ y \\ z \end{pmatrix} = \begin{pmatrix} \cos\alpha & \sin\alpha & 0 \\ -\sin\alpha & \cos\alpha & 0 \\ 0 & 0 & 1 \end{pmatrix} \begin{pmatrix} x \\ y \\ z \end{pmatrix}. \tag{18}$$

To design a coordinate system with an extrapolation direction parallel the propagation direction of the plane-wave source (q_x, q_y, q_z), we rotate the coordinates in two steps. First we rotate about the z-axis by an angle α (equation 18) shown in Figure 1. Second we rotate about the y_1-axis by an angle θ (Figure 2) as follow:

Figure 2: Rotation about the axis y_1 by θ guojian1-rottilt [NR]
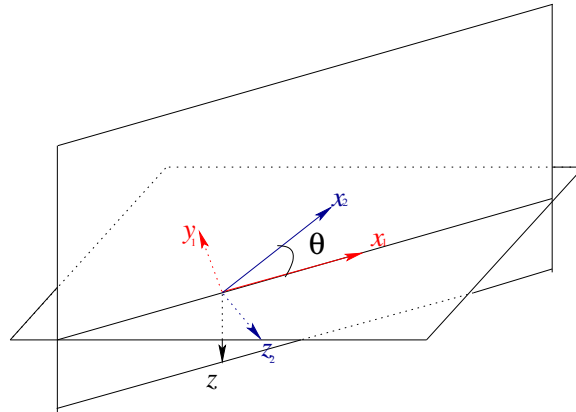
$$\begin{pmatrix} x_2 \\ y_2 \\ z_2 \end{pmatrix} = R_{y_1}(\theta) \begin{pmatrix} x_1 \\ y_1 \\ z_1 \end{pmatrix} = \begin{pmatrix} \cos\theta & 0 & \sin\theta \\ 0 & 1 & 0 \\ -\sin\theta & 0 & \cos\theta \end{pmatrix} \begin{pmatrix} x_1 \\ y_1 \\ z_1 \end{pmatrix}. \tag{19}$$
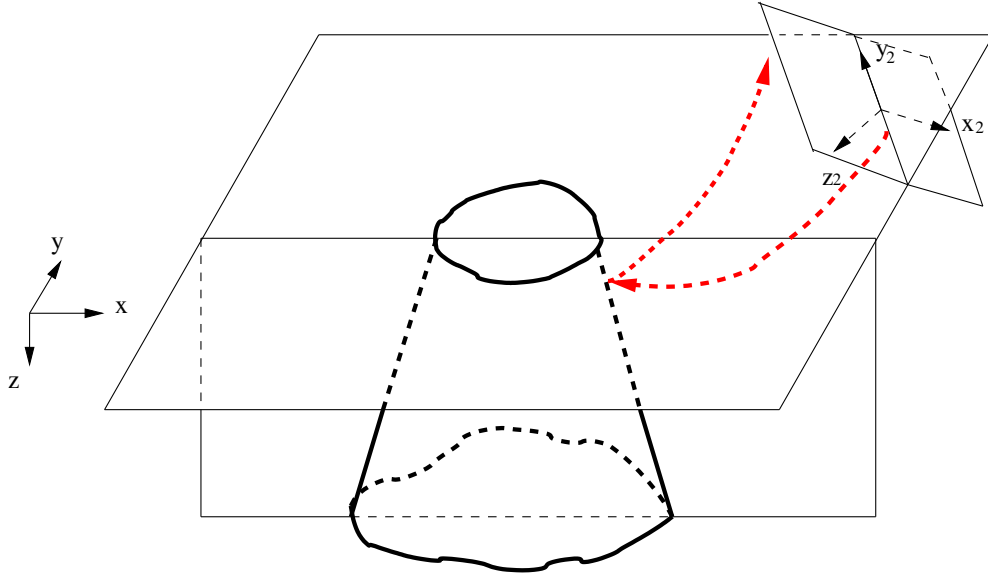
Figure 3: A plane-wave source and its coordinates to image the salt body.(x, y, z) is the original Cartesian coordinates. (x_2, y_2, z_2) is the new tilted coordinates. The dashed line with arrows are the source and receiver rays of the plane-wave source. The extrapolation direction of the new coordinates z_2 axis is closer to the propagation direction of the plane-wave source. guojian1-coordinates [NR]

Combining the two rotations, we have the rotation from original coordinates to the new tilted coordinates as follows,

$$\begin{pmatrix} x_2 \\ y_2 \\ z_2 \end{pmatrix} = \begin{pmatrix} \cos\theta\cos\alpha & \cos\theta\sin\alpha & \sin\theta \\ -\sin\alpha & \cos\alpha & 0 \\ -\sin\theta\cos\alpha & -\sin\theta\sin\alpha & \cos\theta \end{pmatrix} \begin{pmatrix} x \\ y \\ z \end{pmatrix}. \tag{20}$$

It is easy to verify that the depth axis of the new coordinates parallels the propagation direction (q_x, q_y, q_z). In practice, we do not use the direction exactly paralleling the propagation of the plane-wave source at the surface. Considering that the velocity usually increases with the depth, the propagation direction of a plane-wave source becomes increasingly horizontal. So we usually choose a tilting angle θ that is a little bigger than $\arccos(q_z)$.

Figure 3 shows a typical coordinate system used for a plane-wave source to image a salt dome. The dashed lines with arrows show the propagation direction of the source and receiver waves for the plane-wave source. (x, y, z) is the Cartesian coordinate system, and (x_2, y_2, z_2) is the tilted coordinates for the plane-wave source. The extrapolation direction of the new coordinates, which parallels z_2-axis, is much closer to the propagation direction of the plane-wave source than the conventional vertical extrapolation direction.

For conical-wave source migration, we can similarly design tilted coordinates for each conical source. In contrast to the 3D plane-wave source migration, we apply the second rotation directly without rotating the azimuth of the data. Given the conical-wave source with a ray parameter p_x and the surface velocity v_{z0}, we rotate the velocity and the surface data
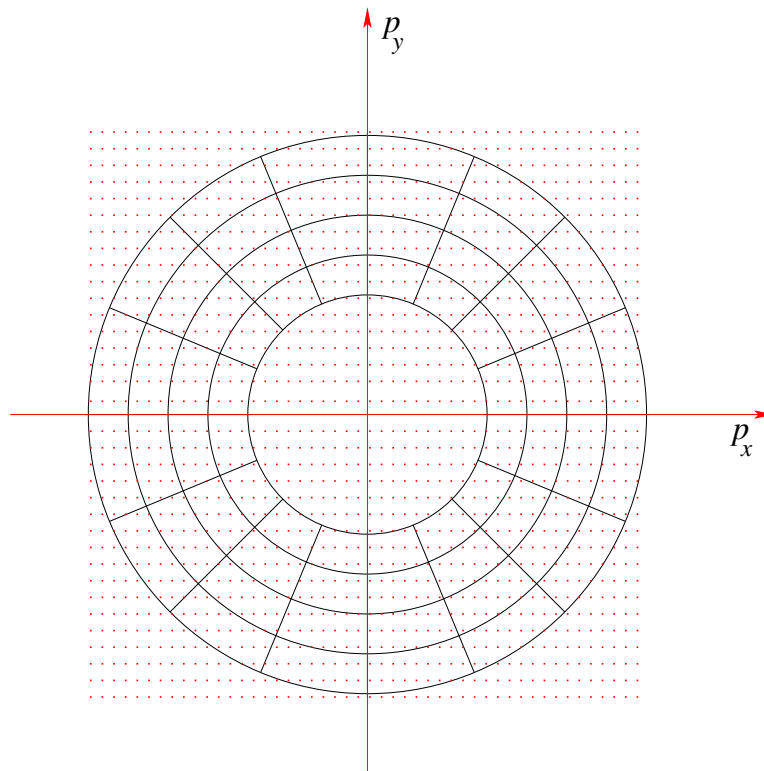
Figure 4: The dots represent all possible plane-wave sources. The circles are the contour of their take-off angles and the smallest circle represents plane-wave sources with a take-off angle of 15°. The radial lines show the contour of azimuth angles. All possible plane-wave sources are divided into small cells. The plane-wave sources in a cell have a similar take-off and azimuth angle and share a coordinate system. guojian1-ppanel [NR]

along y-axis by a angle of $\theta = \arcsin(p_x v_{z0})$ and migrate the data in the new coordinates. This usually works when the in-line direction is the predominant dip direction in the subsurface. When there are steep dips in the cross-line direction, it is still difficult to image these dips with conical-wave migration in tilted coordinates. In contrast, 3D plane-wave migration in tilted coordinates rotate the data and model into a general direction dependent on the propagation direction and it can image these cross-line direction dips.

PRACTICE CONSIDERATIONS

There are three steps to implement plane-wave migration in tilted coordinates for one plane-wave source. First, the source and receiver wavefields are rotated to the new coordinates. Second, for each frequency, source and receiver wavefields are extrapolated into the subsurface and the image is generated by cross-correlating the two wavefields in the new coordinates. Third, the image is rotated back to the original Cartesian coordinates after stacking the images of all the frequencies. In the first step, we rotate a 2D dataset for each frequency, this cost is

trivial compared to the wavefield extrapolation. In the third step, we rotate the 3D image back to Cartesian coordinates after stacking all frequencies, the cost is also very small.

To further reduce the cost of rotations, the plane-wave sources with similar propagation directions share the same tilted coordinate system. This reduces the rotation number in the third step. Figure 4 illustrates how to sample the ray parameters p_x and p_y and how to put plane-wave sources together to share a coordinate system. In Figure 4 we sample (p_x, p_y) in Cartesian coordinates, where p_x, p_y are defined as:

$$p_x = -p_{max}, -p_{max} + dp_x, \cdots, p_{max} - dp_x, p_{max}, \tag{21}$$

$$p_y = -p_{max}, -p_{max} + dp_y, \cdots, p_{max} - dp_y, p_{max}, \tag{22}$$

where p_{max} is defined by the maximum take-off angle and dp_x, dp_y are the sampling of the ray parameters. In Figure 4, each dot represents a plane-wave source with a ray parameter pair (p_x, p_y). Given the surface velocity, we calculate the azimuth angle α and take-off angle θ from (p_x, p_y) and vice versa using equations 16 and 17. Therefore, we can divide the whole area into cells using (α, θ) as the coordinate system. Figure 4 shows the cells in the coordinates (α, θ). All the plane-wave sources whose ray parameter pair (p_x, p_y) fall in a cell share the same coordinate system. The dots in the smallest circle in Figure 4 represent plane-wave sources whose take-off angle θ is smaller than 15°. For those plane-wave sources, we extrapolate its source and receiver wavefields in Cartesian coordinates. For all plane-wave sources whose ray parameter pair (p_x, p_y) is in a cell, we use their average take-off angle and azimuth angle to design the coordinate system for the migration.

ANISOTROPIC MEDIA IN TILTED COORDINATES

It is well known that a VTI (transversely isotropic with a vertical symmetry axis) medium is circularly symmetric in the horizontal plane. Therefore, the medium is still VTI after rotating the azimuth of the model (equation 18). In the second rotation step (equation 19), a VTI medium in Cartesian coordinates changes to a TTI (tilted TI) medium with a constant tilting angle θ in the new coordinates. We keep the y_2-axis in (x, y) plane when we rotate the coordinates. This guarantees the symmetry axis of the new TTI media in the new plane (x_2, z_2). For this kind of TTI media, the dispersion relation is not symmetric in the in-line direction but it is symmetric in the cross-line direction in the new coordinates. The extrapolation operator for this kind of TTI media is simpler than the general TTI media. We need a wavefield-extrapolation operator for TTI media to apply plane-wave migration in tilted coordinates in VTI media. We use optimized implicit finite-difference methods for TTI media (Shan, 2006a). The coefficients for the finite-difference scheme are obtained by fitting the dispersion relation with rational functions.

NUMERICAL EXAMPLES

We test the methodology on a real 3D dataset from the Gulf of Mexico. Figure 5 shows the vertical velocity model with a typical salt body. The salt body is not very complex, but its

flank in both the in-line and cross-line directions are very steep. We obtained the dataset with the velocity and anisotropy parameter models from Exxonmobil. The vertical velocity and anisotropy parameters were estimated by the integrated velocity model estimation (Bear et al., 2005), which incorporates the surface seismic data with all other data available. For this dataset, in addition to vertical check shots and a substantial number of sonic logs, there is an offset check shot survey that serve to constrain the estimation of the velocity and anisotropy parameters. The maximum value of the anisotropy parameters ε and δ are 0.20 and 0.10, respectively.

Figure 6 shows the velocity model we used for migration. We replace the velocity in the salt body with the sediment velocity around it. We migrate 2700 plane-waves in total. The sampling of ray parameter in both in-line and cross-line directions are 0.000013 s/m. And the maximum take-off angle θ is 38°. The samplings for the cells used for sharing tilted coordinates in Figure 4 are $d\theta = 5°$ and $d\alpha = 22.5°$.

For comparison, we did two migrations: anisotropic plane-wave migration in Cartesian coordinates (Shan, 2006b) and anisotropic plane-wave migration in tilted coordinates. Figures 7-10 compare the images of these two migrations at different locations. In these figures, the top panels are the images obtained by anisotropic plane-wave migration in Cartesian coordinates and the bottom ones are the images obtained by anisotropic plane-wave migration in tilted coordinates.

In Figure 7, at "A" in the cross-line section, the top of the salt energy is dim in Figure 7(a) while it is strong and continuous in Figure 7(b). At "B" in the in-line section, the salt flank is well imaged in Figure 7(b) while it is absent in Figure 7(a). At "C" in the depth section, we see the continuous salt boundary from the sediment in Figure 7(b), while we can only see half of it in Figure 7(a).

In Figure 8, at "B" in the in-line section, the salt flank, which is not visible in 8(a) become very evident in Figure 8(b). At "B" in the cross-line section, the salt flank is not imaged at the right position due to the limit of the accuracy of the operator in Figure 8(a) while it is well imaged in Figure 8(b). The salt flank at "D" is strong and continuous in Figure 8(b) but it almost disappears in 8(a). At "C" in the depth section, the salt body can be picked out easily from the sediments in 8(b) but it is not visible in 8(a).

In Figure 9, at "B" in the in-line section, the salt flank , which is not visible in Figure 9(a), is visible in Figure 9(b). The top of the salt in the in-line section in Figure 9(b) is sharper than that in Figure 9(a). In the cross-line section of Figure 9, the plane-wave migration in tilted coordinates images the salt flank at "A" and "D" (Figure 9(b)), which are very weak and not at the right position in Figure 9(a). In the depth section, we can see the salt boundary clearly in 9(b) while they are not visible in Figure 9(a).

In Figure 10 we can see similar improvements of the salt flanks at "A" and "B". At "C", we can also see the steeply dipping faults in Figure 10(b) are much better imaged than that in Figure 10(a).

From these comparisons, we find that plane-wave migration in tilted coordinates greatly improves the images of the salt body and steeply dipping faults.
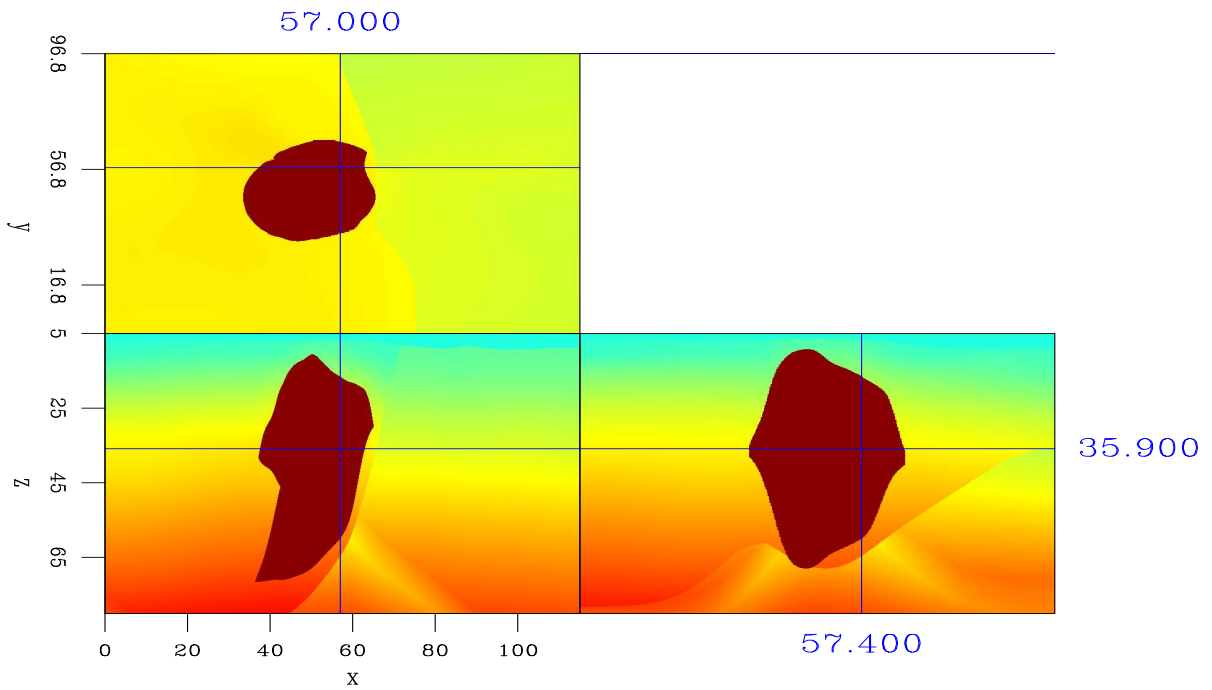
Figure 5: The vertical velocity model of the real dataset. The salt body is not complex but its flanks are steep. guojian1-vel [ER]
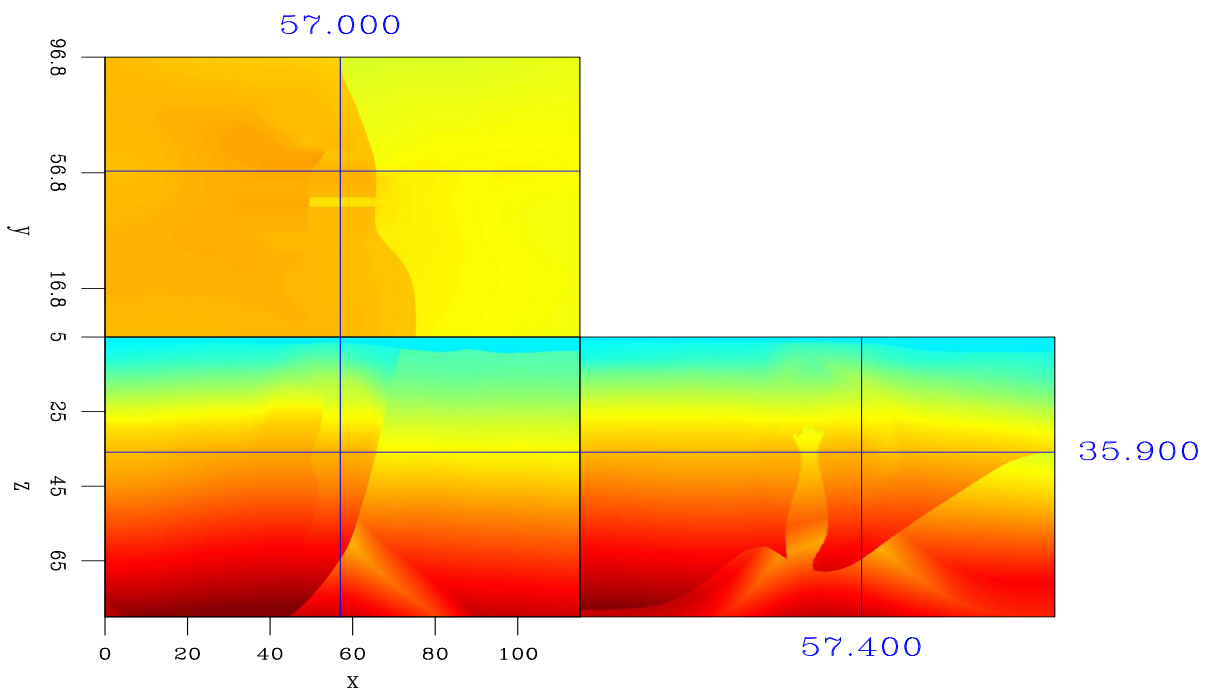

Figure 6: The vertical velocity model used for migration. The salt body is filled with the sediment velocity. guojian1-velnosalt [CR]
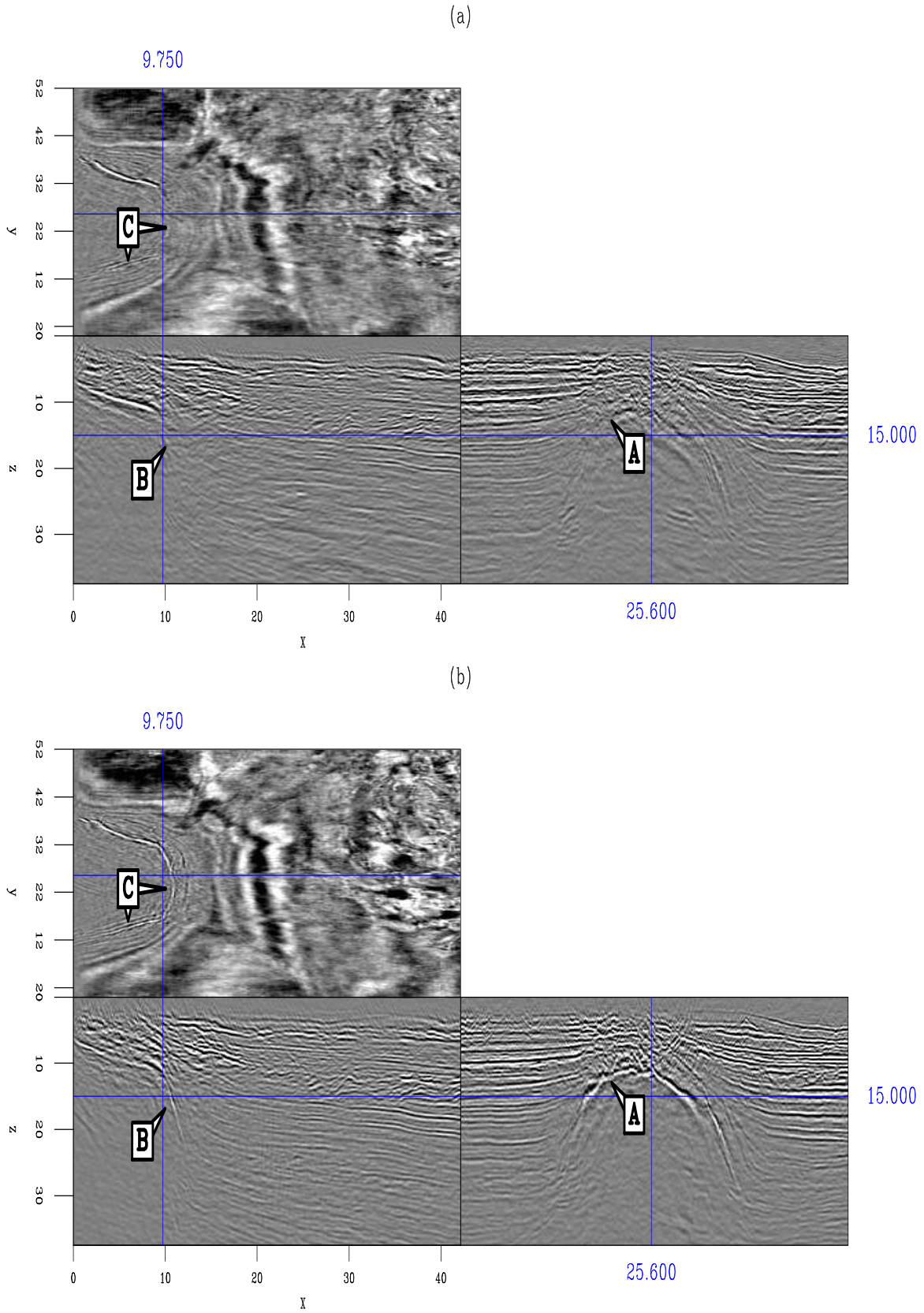
Figure 7: Image comparison: (a) Anisotropic plane-wave migration in Cartesian coordinates; (b) Anisotropic plane-wave migration in tilted coordinates. guojian1-imgcompare1 [CR]
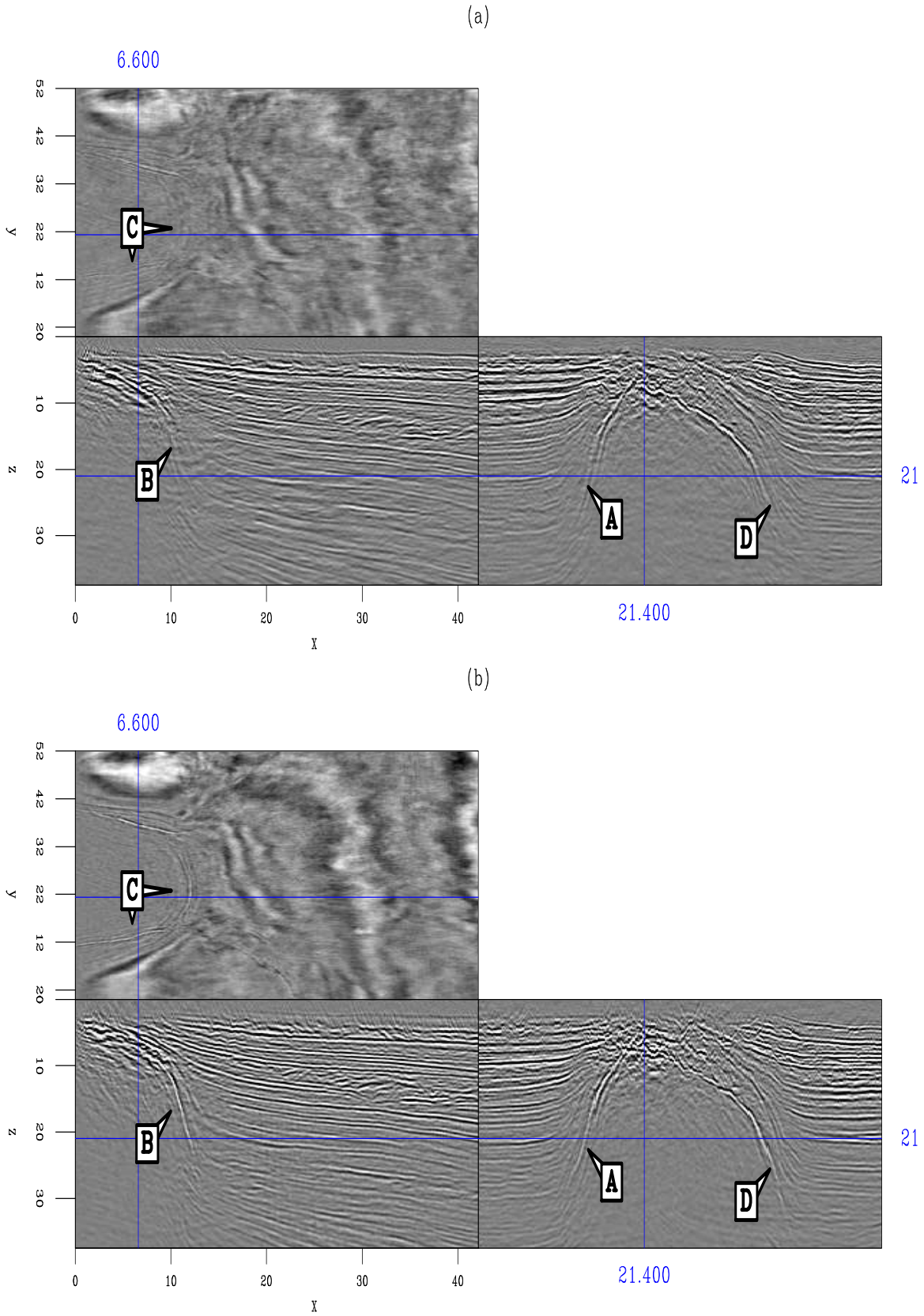
Figure 8: Image comparison: (a) Anisotropic plane-wave migration in Cartesian coordinates; (b) Anisotropic plane-wave migration in tilted coordinates. guojian1-imgcompare2 [CR]
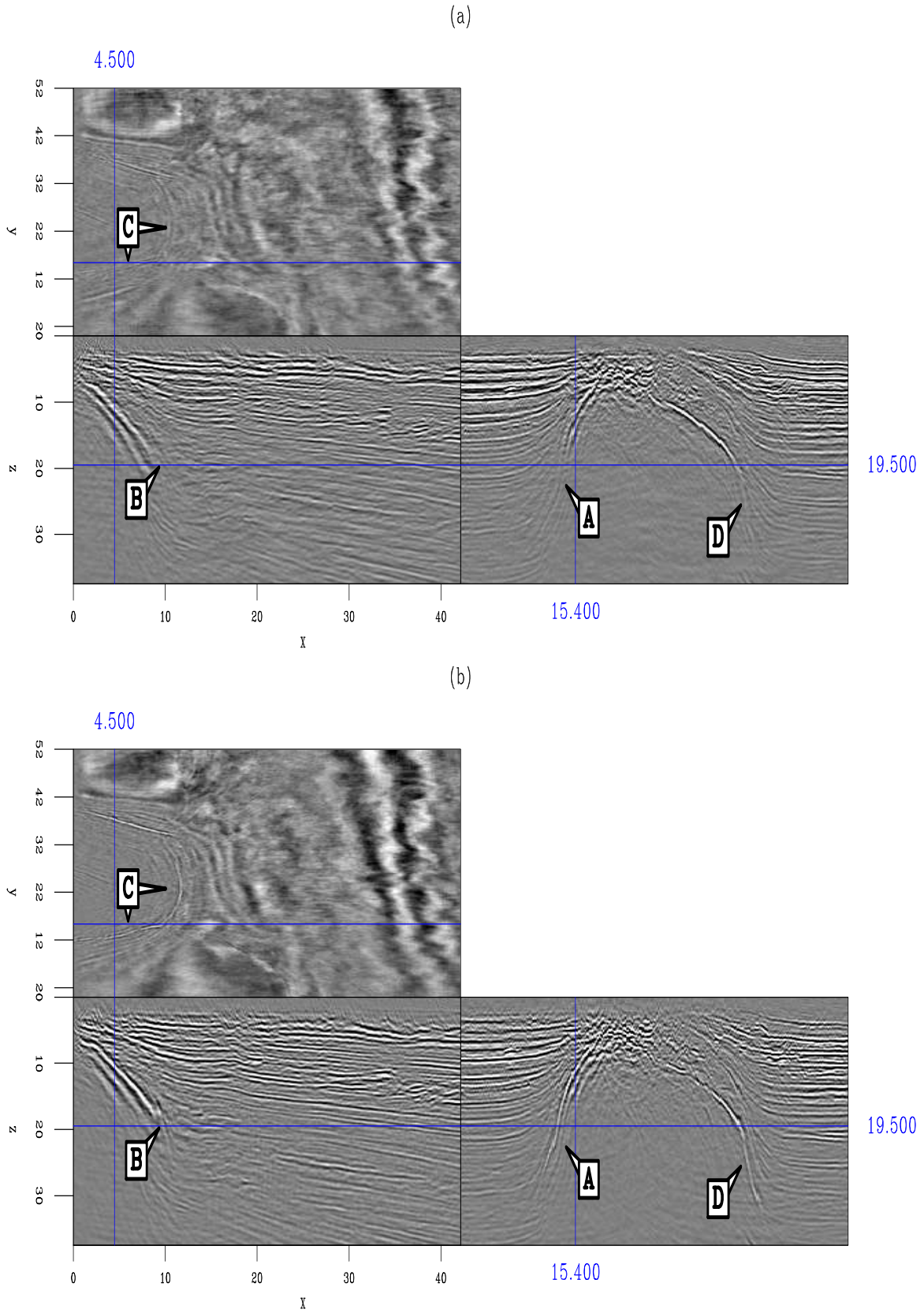
(a)

(b)

Figure 9: Image comparison: (a) Anisotropic plane-wave migration in Cartesian coordinates; (b) Anisotropic plane-wave migration in tilted coordinates. guojian1-imgcompare3 [CR]
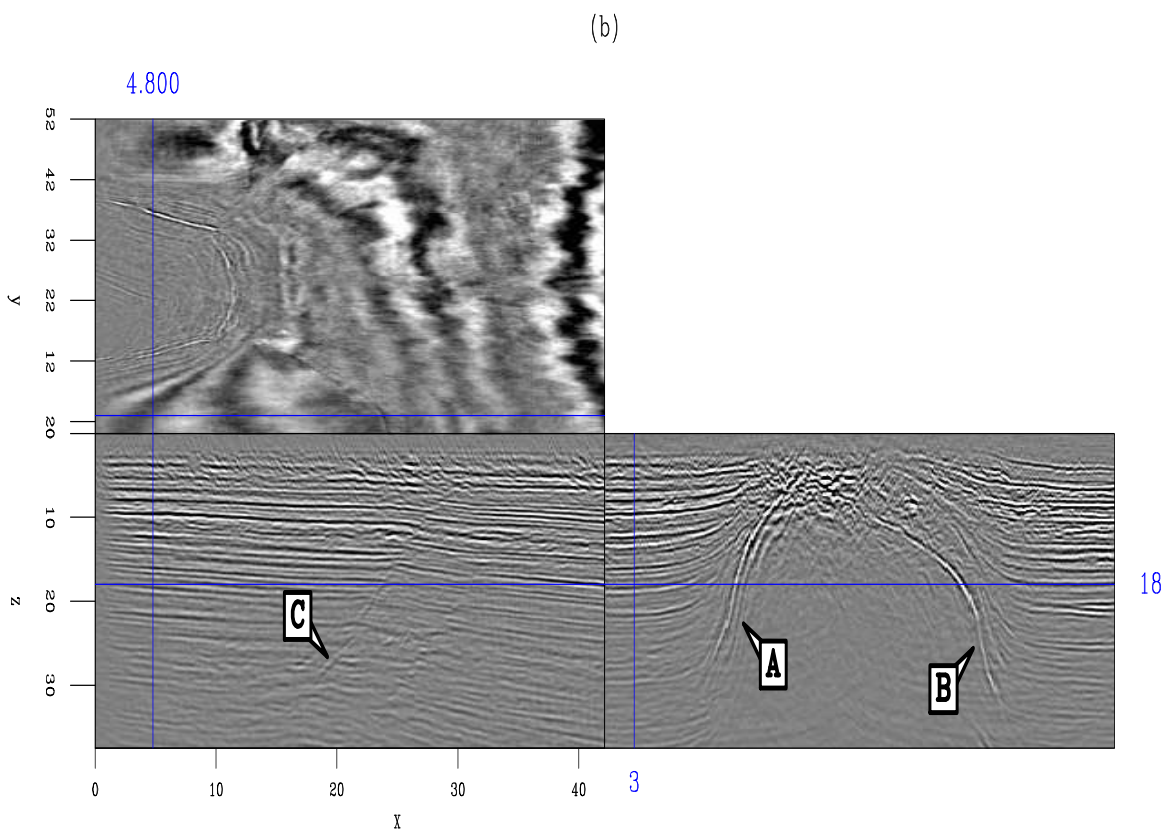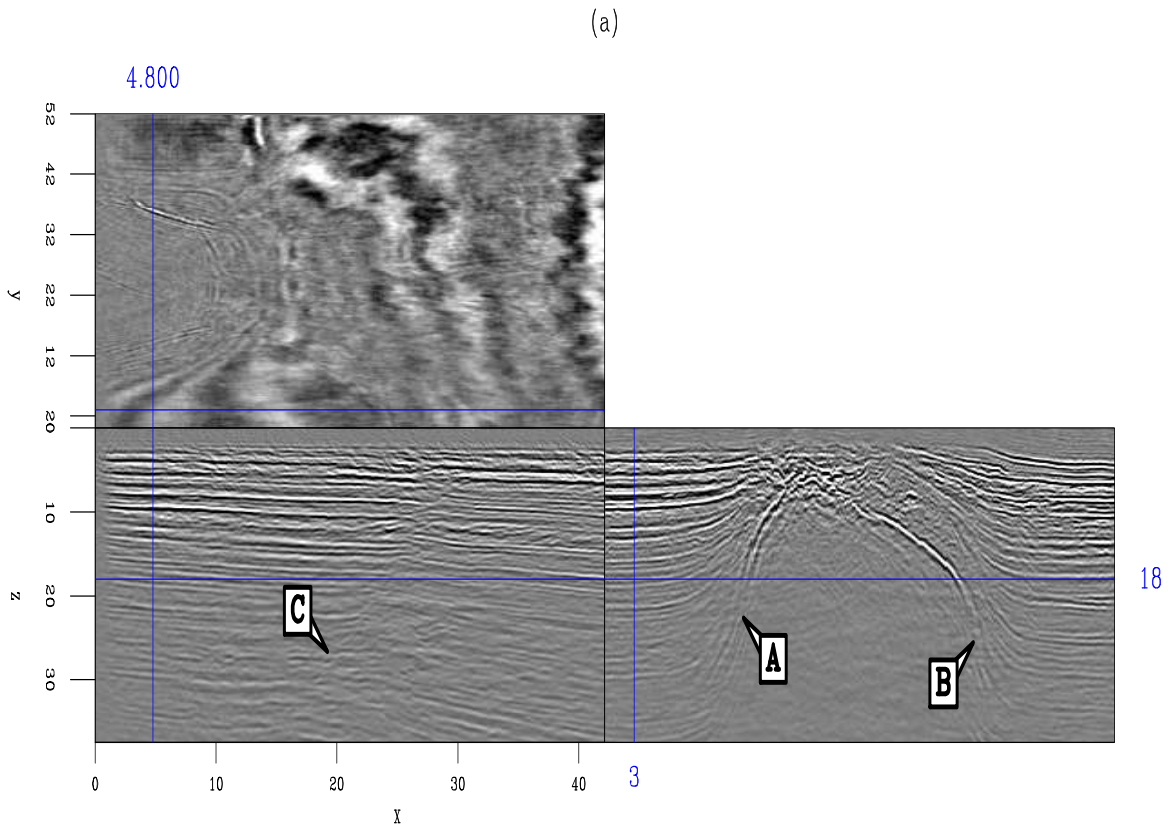
(a)

(b)

Figure 10: Image comparison: (a) Anisotropic plane-wave migration in Cartesian coordinates; (b) Anisotropic plane-wave migration in tilted coordinates. guojian1-imgcompare4 [CR]

CONCLUSION

We present an efficient way to image steeply dipping reflectors and overturned waves using one-way wavefield extrapolation. We decompose the recorded data into plane-wave source data and migrate them using one-way wave equation operator in tilted coordinates. The real dataset examples show that this algorithm effectively images steeply dipping reflectors such as salt body flanks and faults.

ACKNOWLEDGMENTS

REFERENCES

Baysal, E., Kosloff, D. D., and Sherwood, J. W. C., 1983, Reverse time migration: Geophysics, **48**, 1514–1524.

Bear, L., Dickens, T., Krebs, J., Liu, J., and Traynin, P., 2005, Integrated velocity model estimation for improved positioning with anisotropic PsDm: The Leading Edge, **24**, 622–634.

Biondi, B., 2002, Stable wide-angle Fourier finite-difference downward extrapolation of 3-D wavefields: Geophysics, **67**, 872–882.

Biondi, B., and Shan, G., 2002, Prestack imaging of overturned reflections by reverse time migration: Prestack imaging of overturned reflections by reverse time migration, Soc. of Expl. Geophys., 72nd Ann. Internat. Mtg, 1284–1287.

Claerbout, J. F., 1985, Imaging the Earth's Interior: Blackwell Scientific Publications.

Duquet, B., Lailly, P., and Ehinger, A., 2001, 3D plane wave migration of streamer data: 3D plane wave migration of streamer data, Soc. of Expl. Geophys., 71st Ann. Internat. Mtg, 1033–1036.

Etgen, J., 2002, Waves, beams and dimensions: an illuminating if incoherent view of the future of migration: 72nd Ann. Internat. Mtg, Soc. of Expl. Geophys., invited presentation.

Gazdag, J., 1978, Wave equation migration with the phase-shift method: Geophysics, **43**, 1342–1351.

Higginbotham, J. H., Shin, Y., and Sukup, D. V., 1985, Directional depth migration (short note): Geophysics, **50**, 1784–1796.

de Hoop, M. V., 1996, Generalization of the Bremmer coupling series *in* J. Math. Phys. 3246–3282.

Huang, L. Y., and Wu, R. S., 1996, Prestack depth migration with acoustic screen propagators: Prestack depth migration with acoustic screen propagators, Soc. of Expl. Geophys., 66th Ann. Internat. Mtg, 415–418.

Lee, M. W., and Suh, S. Y., 1985, Optimization of one-way wave-equations (short note): Geophysics, **50**, 1634–1637.

Li, Z., 1991, Compensating finite-difference errors in 3-D migration and modeling: Geophysics, **56**, 1650–1660.

Liu, F., Hanson, D. W., Whitmore, N. D., and ann Robert H. Stolt, R. S. D., 2006, Toward a unified analysis for source plane-wave migration *in* Geophysics. S129–S139.

Liu, F., Stolt, R., Hanson, D., and Day, R., 2002, Plane wave source composition: An accurate phase encoding scheme for prestack migration: Plane wave source composition: An accurate phase encoding scheme for prestack migration, Soc. of Expl. Geophys., 72nd Ann. Internat. Mtg, 1156–1159.

Nichols, D., 1994, Imaging in complex structures using band-limited green's function *in* Ph.D. thesis. Stanford University.

Rietveld, W. E. A., 1995, Controlled illumination of prestack seismic migration *in* Ph.D. thesis. Delft University of Technology.

Ristow, D., and Ruhl, T., 1994, Fourier finite-difference migration: Geophysics, **59**, 1882–1893.

Sava, P., and Fomel, S., 2005, Riemannian wavefield extrapolation: Geophysics, **70**, T45–T56.

Shan, G., 2006a, Optimized implicit finite-difference migration for TTI media: SEP– **125**.

—, 2006b, Optimized implicit finite-difference migration for vti media: 76th Ann. Internat. Mtg., Soc. of Expl. Geophys., Expanded Abstracts.

Shan, G., and Biondi, B., 2004, Imaging overturned waves by plane-wave migration in tilted coordinates: 74th Ann. Internat. Mtg., Soc. of Expl. Geophys., Expanded Abstracts, 969–972.

Shragge, J., 2006, Non-orthogonal Riemannian wavefield extrapolation *in* Expanded Abstracts. 75th SEG Ann. Gen. Meeting and Exhibition, 2236–2240.

Whitmore, N. D., 1983, Iterative depth migration by backward time propagation: Iterative depth migration by backward time propagation, Soc. of Expl. Geophys., 53rd Ann. Internat. Mtg, Session:S10.1.

—, 1995, An imaging hierarchy for common angle plane wave seismograms *in* Ph.D. thesis. University of Tulsa.

Zhang, J., and McMechan, G. A., 1997, Turning wave migration by horizontal extrapolation: Geophysics, **62**, 291–297.

Zhang, Y., Sun, J., Notfors, C., Gray, S., Chernis, L., and Young, J., 2005, Delayed-shot 3D depth migration: Geophysics, **70**, E21–E28.